Protection and Control of
Modern Power Systems

**ORIGINAL RESEARCH**                                                        **Open Access**

# A robust model-free controller for a three-phase grid-connected photovoltaic system based on ultra-local model

Ahsene Boubakir[1*] , Sid-Ahmed Touil[2], Salim Labiod[1] and Nasserdine Boudjerda[3]

**Abstract**

In this paper, a robust model-free controller for a grid-connected photovoltaic (PV) system is designed. The system consists of a PV generator connected to a three-phase grid by a DC/AC converter. The control objectives of the overall system are to extract maximum power from the PV source, to control reactive power exchange and to improve the quality of the current injected into the grid. The model-free control technique is based on the use of an ultra-local model instead of the dynamic model of the overall system. The local model is continuously updated based on a numerical differentiator using only the input–output behavior of the controlled system. The model-free controller consists of a classical feedback controller and a compensator for the effects of internal parameter changes and external disturbances. Simulation results illustrate the efficiency of the controller for grid-connected PV systems.

**Keywords:** Photovoltaic system, Maximum power point, Model-free control, Ultra-local model, Numerical differentiator

## 1 Introduction

Solar energy is considered as one of the best sources of renewable energy to address the energy crisis and to reduce the level of pollution caused by the use of fossil fuels. Photovoltaic (PV) generator systems are used to directly and efficiently convert solar energy to electricity at low cost and can be classified as autonomous or stand-alone systems [1–3] and grid connected systems [4–6]. They have been used primarily as stand-alone systems in locations where utility lines are not available, such as in mountains, islands and isolated sites, or in areas where installing utility lines is not economical. A stand-alone system requires batteries to store the energy supplied by the solar panels, so the batteries must be properly sized to obtain maximum efficiency from the PV generators. This increases the volume and cost of such installations

[1, 2]. Unlike autonomous systems, grid-connected PV systems allow direct injection of energy produced by solar panels into the grid [4, 5].

The overall efficiency of grid-connected PV systems is influenced by climatic factors such as solar radiation and temperature, as well as the converters and controllers being used. Since the weather factors are out of users' control, the choice of converter and controller design plays a key role in the performance of the overall system. The role of a power converter in a grid-connected PV system is to perform the energy transfer between the PV panels and the electrical grid. There are generally two main topologies depending on the number and type of the converters used [4, 5]. In the first, referred to as double stage PV systems, the grid and the PV panels are connected via a DC/DC power converter, functioning as a maximal power point tracker (MPPT), and a DC/AC converter used for feeding power back to the grid and power factor correction (PFC). The second is the single stage PV systems [4], in which the grid and the PV panels

*Correspondence: ah_boubakir@yahoo.fr
[1] LAJ, Faculty of Science and Technology, University of Jijel, BP. 98, Ouled Aissa, 18000 Jijel, Algeria
Full list of author information is available at the end of the article

are directly connected by a DC/AC converter providing MPPT, power transfer, and PFC requirements.

The efficient use of PV energy has attracted a lot of attention in the fields of renewable energy, electrical engineering, control engineering etc. The main control objectives in a grid-connected PV system are: i) feeding the extracted maximum power from the PV generator to the grid under various environmental conditions, ii) control of reactive power injected into the grid, and iii) minimization of the harmonic distortion in the current fed to the grid.

Design of control techniques for grid-connected PV systems has been much studied over the past years and remains an active area of research. Traditional fixed-gain linear controllers such as PI/PID controllers [7, 8] and repetitive controllers (RC) [9] have been widely used, while recent advances in control theory have enabled the development of other more effective control algorithms. In [4], an input output feedback linearization control scheme is proposed, one transforms the overall dynamics of the grid-connected PV system into two equivalent linear subsystems, to allow the use of the pole placement linear control technique. A robust feedback linearizing control strategy is suggested in [5] based on a sliding mode compensator to enhance robustness against uncertainties. In [10], a robust model predictive control is proposed to control a grid-connected PV system using a disturbance compensator with an integral action, while another robust control method is introduced in [11] consisting of an active disturbance rejection control law combined with an RC term and designed by solving linear matrix inequality constraints. In [12], an offset-free feedback linearization controller based on a PI/almost PID disturbance observer is presented. Other control strategies can also be found in the literature such as second-order sliding model [13, 14], fuzzy logic [15–17], robust [18, 19], the backstepping technique [6, 20] and predictive [21, 22]. The majority of control laws proposed in the aforementioned works and other literature are either fixed-gain linear [7, 8], model-based [4, 5, 10], or control methods based on artificial intelligence tools such as fuzzy logic or neural networks [15–17, 23]. Unfortunately, a conventional fixed-gain linear controller cannot efficiently handle dynamic operating conditions or cope with external disturbances. In addition, the performance of a model-based controller is highly dependent on obtaining a good dynamic model of the system and its operating environment along with knowledge of the external disturbances that influence its behavior. It is usually difficult to meet these needs. Although the learning capacities of artificial intelligence tools help in the approximation of uncertainties, they complicate the structure of the control laws and their real-time implementation. In addition, the closed-loop performance of a controller based on artificial intelligence tools depend upon designer skills.

In this work, a Model-Free Controller (MFC) based on an elementary continuously updated local model is designed for a grid-connected PV system. An ultra-local model valid over a short period of time is used to instantly identify the overall system dynamics, while the adopted local model is continuously updated using only the input–output behavior of the system with an online numerical differentiator. The derived control law consists of a classical feedback controller and a compensator which compensates for the effects of internal parameter changes and external disturbances. The model-free control approach proposed presents a more effective solution in grid-connected PV system control than previously cited control methods. It offers users a universal and robust controller that easily adapts to the external environment and its changes. The key advantages of the proposed control and the contributions of the paper include:

1. Unlike the majority of existing approaches, the proposed control scheme can control the power factor and the DC-link voltage with the same control algorithm. Thus there is no need to carry out the control of these variables with two separate algorithms.
2. The MPP tracking is achieved by controlling the DC/AC converter. This eliminates the need for a DC-DC converter.
3. The control law is derived directly from a general model of grid-connected PV systems and its implementation does not require knowledge of the model. This means that the designed controller can be regarded as a universal model-free controller for grid-connected PV systems.
4. The instantaneous identification of the overall dynamics significantly improves the robustness of the MFC controller against internal parameter changes (e.g., filter parameters or grid electrical quantities) and external disturbances (e.g., atmospheric conditions).
5. In contrast to the existing model-free controls of grid-connected PV systems such as the conventional fixed-gain linear controllers and methods based on artificial intelligence tools (e.g., fuzzy logic, neural networks or optimization techniques), the proposed model-free control is easy to implement, robust and self-adjusting.

The rest of this paper is organized as follows. Section 2 gives the description and mathematical modeling of the grid-connected PV system. The principle of the model-free control technique based on instantaneous
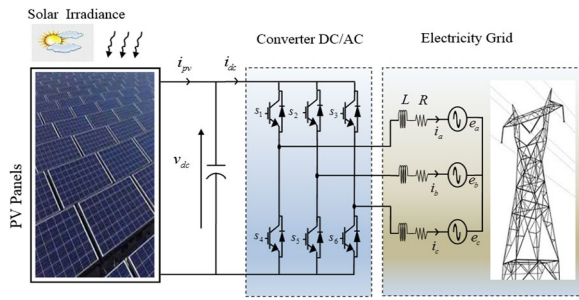
**Fig. 1** Schematic diagram of the grid-connected PV system



**Fig. 2** Equivalent circuit of a PV cell

identification is introduced in Sect. 3, while model-free control design for the grid-connected PV system and the analysis of the simulation results are detailed in Sect. 4. Finally, Sect. 5 concludes the paper.

## 2 Description and modeling of the grid-connected PV system

The structure of the grid-connected PV system is displayed in Fig. 1. It includes a PV generator, a DC-link capacitor, and a three-phase two-level converter connected to the grid via an inductive output filter. The role of the DC-link capacitor in this single-stage configuration is to maintain the voltage at the input of the converter within an acceptable operating range. The converter, with its control mechanism, regulates the DC-link voltage to a desired level and synchronizes the converter output current with the grid voltage to achieve unity power factor. The filter enhances the quality of the current injected into the grid by reducing harmonic pollution.

To facilitate the design of the system controller, a detailed mathematical representation of all the parts of the system is derived. It is worth noting that for the proposed control scheme, the knowledge of the system model is not required for its real-time implementation as it is in conventional model-based controllers.

### 2.1 PV array modeling

PV cells are the basic components of all PV generator systems. A PV cell is a p–n junction able to convert sunlight directly to electric power. The equivalent circuit of a PV cell is shown in Fig. 2. It is composed of a light generated current source in parallel with a diode, a series resistance $R_s$ and a shunt resistance $R_{sh}$ that characterize respectively the series connecting circuit and the losses in the PV cell as parallel current leakage. A single PV cell can only provide a small amount of energy, so a number of cells are assembled in series–parallel combination to make a PV module with higher current and voltage. A PV generator is constituted of PV modules connected in series and in parallel to obtain the desired output power.
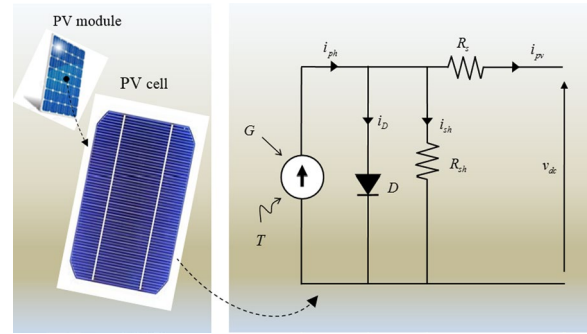
From the equivalent circuit in Fig. 2, there is:

$$i_{pv} = i_{ph} - i_D - i_{sh} \tag{1}$$

where $i_{ph}$ is the photocurrent whose intensity depends on irradiance $G$ and temperature $T$, $i_D$ is the current through the diode and $i_{sh}$ is the current flowing through the resistor $R_{sh}$.

The relationship between the output current $i_{pv}$ and voltage $v_{dc}$ for a PV cell can be detailed as [1, 19, 24, 25]:

$$i_{pv} = i_{ph} - I_0 \left[ \exp \left( q \frac{\left(v_{dc} + R_s i_{pv}\right)}{nKT} \right) - 1 \right] + \frac{v_{dc} + R_s i_{pv}}{R_{sh}} \tag{2}$$

where $I_0$ is the cell reverse saturation current that depends on temperature $T$, $q$ is the electron charge $\left( q = 1.6 \times 10^{-19} C \right)$, $n$ is the quality factor of the diode, $K$ is the Boltzman's constant $\left( K = 1.38 \times 10^{-23} \text{ J/K} \right)$ and $T$ is the cell temperature.

Note that the shunt resistance $R_{sh}$ in the equivalent circuit is large and its effect can be neglected in (2), as it only affects very low levels of solar irradiation [25]. The output current $i_{pv}$ and voltage $v_{dc}$ of a PV module/array, that includes $N_s$ series cells and $N_p$ parallel cells, can be deduced from (2) as [1, 4, 25]:

$$i_{pv} = N_p i_{ph} - N_p I_0 \left[ \exp \left( \frac{q}{nKT} \left( \frac{v_{dc}}{N_s} + \frac{R_s i_{pv}}{N_p} \right) \right) - 1 \right] \tag{3}$$

$$i_{ph} = \left( i_{sc} + k_i \left( T - T_{ref} \right) \right) \frac{G}{1000} \tag{4}$$

$$I_0 = I_{0R} \left( \frac{T}{T_{ref}} \right)^3 \exp \left( \frac{q E_g}{nK} \left( \frac{1}{T_{ref}} - \frac{1}{T} \right) \right) \tag{5}$$

where $i_{sc}$ is the short circuit current at reference temperature $T_{ref}$ and radiation, and $I_{0R}$ is the cell reverse saturation current at the reference temperature. $k_i$ is the short circuit current temperature coefficient, $G$ is the total

solar radiation in $\text{W/m}^2$ and $E_g$ is the band gap of the semiconductor used in the cell.

The selection of solar panels for PV generator systems is generally done according to the type of PV cells used and their efficiencies, short circuit current, open circuit voltage, optimal operating point and fill factor. The PV array size is designed based on the power requirement of the grid, and consists of strings of PV modules in series and in parallel. In this study, the BP3160 module [18, 26, 27] is chosen and is made of 72 multi-crystalline silicon solar cells connected in series and is able to provide 160 watts of nominal maximum power. The parameters of the BP3160 module in standard conditions (1 $\text{kW/m}^2$ and 25 °C) are shown in Table 1, and the I–V and P–V characteristics for different levels of solar radiation and temperature can be found in [18]. The PV generator system here has 5 strings, each containing 30 PV modules.

## 2.2 Three-phase grid-connected PV system modelling

In the following, the mathematical modeling of the dynamics of the three-phase grid-connected PV system is presented, and is composed of a PV module, a capacitive DC-link, a three-phase two-level converter and a three-phase grid with inductive output filter. First, the dynamic equations of the grid current are written as:

$$\begin{cases} \dfrac{di_a}{dt} = -\dfrac{R}{L}i_a - \dfrac{1}{L}e_a + \dfrac{1}{L}v_a \\ \dfrac{di_b}{dt} = -\dfrac{R}{L}i_b - \dfrac{1}{L}e_b + \dfrac{1}{L}v_b \\ \dfrac{di_c}{dt} = -\dfrac{R}{L}i_c - \dfrac{1}{L}e_c + \dfrac{1}{L}v_c \end{cases} \quad (6)$$

where $v_a$, $v_b$ and $v_c$ are the three-phase voltages at the output of the converter, $i_a$, $i_b$ and $i_c$ represent the three-phase currents injected into the grid, $e_a$, $e_b$ and $e_c$ are the three-phase grid voltages, and $R$ and $L$ are the total resistance and inductance of the line filter. Considering uncertainties, the dynamics of the three-phase converter can be represented in the dq rotating reference frame as:

**Table 1** Specifications of PV module BP3160 [26]

| Parameter | Notation | Numerical value |
| --- | --- | --- |
| Peak power | $P_{max}$ | 160 W |
| Voltage at peak power | $V_{mp}$ | 34.5 V |
| Current at peak power | $I_{mp}$ | 4.55A |
| Short-circuit current | $i_{sc}$ | 4.8A |
| Open circuit voltage | $V_{oc}$ | 44.2 V |
| Number of cells | $N_s$ | 72 |

$$\begin{cases} \dfrac{di_d}{dt} = -\dfrac{R}{L}i_d + wi_q - \dfrac{e_d}{L} + \dfrac{1}{L}v_d + \dfrac{1}{L}\varphi_d \\ \dfrac{di_q}{dt} = -\dfrac{R}{L}i_q - wi_d - \dfrac{e_q}{L} + \dfrac{1}{L}v_q + \dfrac{1}{L}\varphi_q \end{cases} \quad (7)$$

where $i_d$ and $i_q$ are the respective d-axis and q-axis currents, $v_d$ and $v_q$ denote the d-axis and q-axis components of the converter output voltage, $e_d$ and $e_q$ are the d-axis and q-axis components of the grid voltage, respectively. $w = 2\pi f$ where $f$ is the grid frequency, and $\varphi_d$ and $\varphi_q$ denote the disturbance terms such as unmodeled dynamics and exogenous disturbances.

The DC side of the converter is governed by the following dynamics equation:

$$C\frac{dv_{dc}}{dt} = i_{pv} - i_{dc} \quad (8)$$

where $v_{dc}$ is the DC-link voltage, $i_{dc}$ is the DC input current to the converter, $i_{pv}$ is the PV array output current and $C$ is the DC-link capacitance. When the power losses in the electronic switches are neglected, the power balance relationship between the input and output of the converter can be expressed as:

$$v_{dc}i_{dc} = \frac{3}{2}\left(e_d i_d + e_q i_q\right) \quad (9)$$

Substituting $i_{dc}$ in (8) by its expression derived from (9) yields:

$$C\frac{dv_{dc}}{dt} = i_{pv} - \frac{3}{2}\frac{e_d i_d + e_q i_q}{v_{dc}} \quad (10)$$

Considering the system uncertainties, (10) can be rewritten as:

$$\frac{dv_{dc}}{dt} = -\frac{3}{2Cv_{dc}}\left(e_d i_d + e_q i_q\right) + \frac{1}{C}i_{pv} + \frac{1}{C}\varphi_v \quad (11)$$

where $\varphi_v$ represents the system uncertainties and external disturbances.

Finally, the overall dynamics of the controlled system are given by:

$$\begin{cases} \dfrac{di_d}{dt} = -\dfrac{R}{L}i_d + wi_q - \dfrac{e_d}{L} + \dfrac{1}{L}v_d + \dfrac{1}{L}\varphi_d \\ \dfrac{di_q}{dt} = -\dfrac{R}{L}i_q - wi_d - \dfrac{e_q}{L} + \dfrac{1}{L}v_q + \dfrac{1}{L}\varphi_q \\ \dfrac{dv_{dc}}{dt} = -\dfrac{3}{2Cv_{dc}}\left(e_d i_d + e_q i_q\right) + \dfrac{1}{C}i_{pv} + \dfrac{1}{C}\varphi_v \end{cases} \quad (12)$$

In the dq rotating reference frame, the active and reactive powers, $P$ and $Q$, injected into the grid can be described by [13, 17]:

$$P = \frac{3}{2}\left(e_d i_d + e_q i_q\right)$$
$$Q = \frac{3}{2}\left(-e_d i_q + e_q i_d\right) \tag{13}$$

Assuming that the rotation of the dq reference frame is synchronized with the grid voltage vector [13], i.e., $e = e_d + j0$, then (13) becomes:

$$P = \frac{3}{2}(e_d i_d)$$
$$Q = \frac{3}{2}\left(-e_d i_q\right) \tag{14}$$

From (14), it is possible to minimize the reactive power $Q$ by forcing the q−axis line current $i_q$ to zero.

In the next section, the basic principles of the model-free control technique and the different structures of the intelligent PID controller will be presented.

## 3 Model-free control technique

Over the last decade, the design of model-free control schemes based on a continuously updated local model, and the so-called intelligent PID controllers or i-PID, has been an active area of research, because of the importance of these controllers in industrial control systems [28–30]. The main idea is to control a given unknown plant as a simple linear system of order $\upsilon$. This is a local nonphysical model and the so-called ultra-local model. It represents an instantaneous identification of the overall dynamics of the controlled system.

### 3.1 Ultra-local model

The input–output behavior of a controlled plant, even if it is highly nonlinear and time-varying, can be well approximated within its operating range by an unknown finite-dimensional ordinary differential equation in the form of:

$$E\left(y, \dot{y}, \ldots, y^{(a)}, u, \dot{u}, \ldots, u^{(b)}\right) = 0 \tag{15}$$

where $u$ and $y$ are the input and output variables of the system, $E$ is assumed to be a sufficiently regular function of its arguments, while $a$ and $b$ are the derivative orders of output $y$ and input $u$, respectively.

Now, suppose that for an integer $\upsilon$, $0 < \upsilon \leq a$, there is $\frac{\partial E}{\partial y^{(\upsilon)}} \neq 0$. Thus, according to the implicit function theorem [31, 32], the system in (15) can locally be rewritten as:

$$y^{(\upsilon)} = \mathbb{Q}\left(y, \dot{y}, \ldots, y^{(\upsilon-1)}, y^{(\upsilon+1)}, \ldots, y^{(a)}, u, \dot{u}, \ldots, u^{(b)}\right) \tag{16}$$

The principle of the model-free control method (as shown in Fig. 3), proposed by Fliess et al. [28, 29], is to
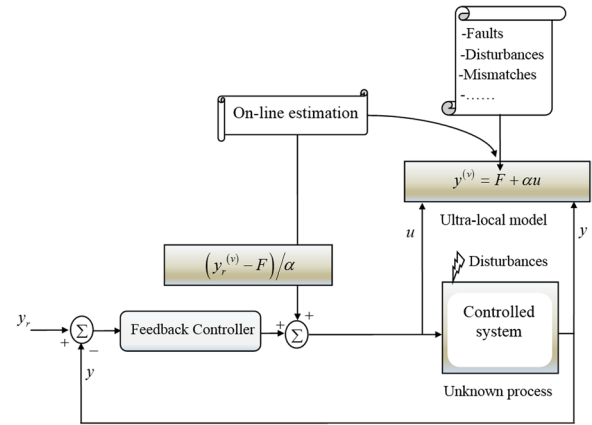


**Fig. 3** Principle of the model-free control method

replace (16) by a phenomenological ultra-local model which is valid only during a very short time interval, as:

$$y^{(\upsilon)} = F + \alpha u \tag{17}$$

where $F$ includes the unmodeled system dynamics, the parametric uncertainty and the external disturbances. $\alpha \in \mathbb{R}$ is a non-physical constant parameter. Users can choose the value of $\alpha$ by trial and error such that $F$ and $\alpha u$ are of the same magnitude.

*Remark 1* The order of derivative $\upsilon$ in (17) is not necessarily equal to the order of derivative $a$ of output $y$ in (16). Usually, the design parameter $\upsilon$ is selected as $\upsilon = 1$ or 2 independently of the system order [29, 30]. In addition, according to (17), knowledge of only $y^{(\upsilon)}$, $u$ and $\alpha$ is sufficient to determine the value of $F$ at each instant of time.

For control purposes, the term $F$ in (17) is assumed to be a piecewise constant function and its estimate is denoted as $\hat{F}$, which is continuously updated as:

$$\hat{F} = \hat{y}^{(\upsilon)} - \alpha u \tag{18}$$

where $\hat{y}^{(\upsilon)}$ is the estimate of $y^{(\upsilon)}$.

### 3.2 Principle and structure of model-free control

To force the output $y$ of a controlled plant, as in (15) and (17), to follow a given smooth reference trajectory $y_r$, the input $u$ can be designed as:

$$u = \frac{1}{\alpha}\left(y_r^{(\upsilon)} - \hat{F} + \Lambda(e)\right) \tag{19}$$

with $e = y_r - y$ as the tracking error. $\Lambda(e)$ is a function that should be selected so that the desired closed-loop behavior $e^{(\upsilon)} + \Lambda(e) = 0$ is asymptotically stable, where $\Lambda(e) = K_{\upsilon-1}e^{(\upsilon-1)} + \cdots + K_1\dot{e} + K_0e$. In fact, the term

Boubakir *et al. Protection and Control of Modern Power Systems* (2021) 6:43

Page 6 of 13

$\Lambda(e)$ in (19) represents a classical feedback controller, chosen by the operator, and the component $\frac{1}{\alpha}\left(y_r^{(v)} - \hat{F}\right)$ is for cancelling the influence of the unmodeled system dynamics and the external disturbances.

The substitution of (19) in (17) gives the following for the tracking error $e$:

$$e^{(v)} + \Lambda(e) + \left(F - \hat{F}\right) = 0 \tag{20}$$

Therefore, a model-free controller in the form (19) can ensure the asymptotic stability of the closed-loop system if $F$ is well estimated such that $F - \hat{F} \approx 0$.

### 3.3 Intelligent-PID controllers

Several control methods can be used in (19) to design the feedback controller $u_{feedback} = \Lambda(e)$. This is connected to the model-free nonlinearity compensator, i.e., $u^* = \frac{1}{\alpha}\left(y_r^{(v)} - \hat{F}\right)$, to form the model-free control law. Generally, the PID controller is the one most used as a feedback controller because of its simple structure and ease of implementation. A model-free control law in the form (19) with a PID feedback controller is called intelligent PID or i-PID.

When selecting the order of derivative $v = 2$ in (17), the control objective can be achieved by the intelligent controllers i-PID or i-PD given by:

$$u = \frac{1}{\alpha}\left(\ddot{y}_r - \hat{F} + \Lambda(e)\right) \tag{21}$$

$$(i - PID)\, \Lambda(e) = K_p e + K_I \int e + K_d \dot{e} \tag{22}$$

$$(i - PD)\, \Lambda(e) = K_p e + K_d \dot{e} \tag{23}$$

where $K_p$, $K_I$ and $K_d$ denote the proportional, derivative and integral gains, respectively. On the other hand, an intelligent Proportional Integral (i-PI) controller or an intelligent Proportional (i-P) controller can be designed when $v = 1$ in (17), such that:

$$(i - PI)\, \Lambda(e) = K_p e + K_I \int e \tag{24}$$

$$(i - P)\, \Lambda(e) = K_p e \tag{25}$$

*Remark 2* The i-P and i-PD controllers are the two most widely used intelligent controllers in control system applications. In the light of the study in [33], the i-P and i-PD controllers are very efficient, unlike i-PI and i-PID controllers which play an imaginary role. Moreover, a certain equivalence exists between i-PD and the usual

PID as demonstrated in [29, 34]. Hence, the i-PD controller is suggested as a good replacement for the conventional PID controller.

### 3.4 Algebraic estimation of *F*

The estimate $\hat{F}$ of the unknown function $F$ plays an important role in the performance of both the general model-free controller in (19) and intelligent controllers in (22)-(24). According to (17), to properly estimate $F$, $y^{(v)}$ requires reconstruction a priori. Since the measurements are usually noisy in real-time applications, it is evident that the accurate estimation of $F$ is highly dependent on an efficient numerical differentiator $\hat{y}^{(v)}$, which is insensitive to measurement noise. The numerical differentiators derived from the Algebraic Differentiation Estimation (ADE) [35–37] are widely used in model-free control, because of their efficiency and integral structure. These numerical differentiators of noisy signals are designed by resolving a classical polynomial approximation of signals, resulting from an algebraic manipulation of signals in the operational domain, as detailed in [36].

*Remark 3* It is worth pointing out that the previous control inputs are used to compute the estimate $\hat{F}$ in (18) in order to avoid any algebraic loop. Thereby, $\hat{F}$ can be computed as:

$$\hat{F} = \hat{y}^{(v)} - \alpha u(t - h) \tag{26}$$

where $u(t - h)$ is delayed control while the delay $h$ is sufficiently small and whose value can be chosen equal to one or a few sampling instants.

## 4 Model-free control applied to the grid-connected PV system

The purpose of this part of the paper is to apply and verify the efficiency of the model-free control technique discussed in the previous section for a grid-connected PV system. A comparative study with conventional controllers is carried out to highlight the performance of the developed controller. A model-free controller is designed for the grid-connected PV system based on ultra-local models derived from the overall dynamic model of the system, which contains uncertainties and is subjected to external disturbances.

### 4.1 Control objectives

The control objectives for the grid-connected PV system are to extract the maximum power from the PV generator system regardless of atmospheric conditions, to control the reactive power injected into the grid and to improve

the quality of the grid current. For this system, the maximum power extraction can be achieved by forcing the DC-link voltage $v_{dc}$ to follow its reference computed by the MPPT tracker, while the control of the reactive power injected into the grid can be fulfilled by controlling $i_q$ of the grid current. Hence, $y_1 = v_{dc}$ and $y_2 = i_q$ are selected as the controlled outputs for the system.

The state representation of (12) can be expressed as:

$$\begin{cases} \dot{x} = f(x) + g(x)u \\ y = [x_3, x_2]^T \end{cases} \tag{27}$$

where $[x_1, x_2, x_3]^T = [i_d, i_q, v_{dc}]^T$ denotes the state space vector, $u = [u_1, u_2]^T = [v_d, v_q]^T$ is the vector of the control inputs. $f(x)$ and $g(x)$ are two vector fields defined by:

$$f(x) = \begin{bmatrix} f_1(x) \\ f_2(x) \\ f_3(x) \end{bmatrix} = \begin{bmatrix} -\dfrac{R}{L}x_1 + wx_2 - \dfrac{e_d}{L} + \dfrac{1}{L}\varphi_d \\ -\dfrac{R}{L}x_2 - wx_1 - \dfrac{e_q}{L} + \dfrac{1}{L}\varphi_q \\ \dfrac{1}{C}i_{pv} - \dfrac{3}{2C}\dfrac{e_dx_1 + e_qx_2}{x_3} + \dfrac{1}{C}\varphi_v \end{bmatrix} \tag{28}$$

$$g(x) = \begin{bmatrix} \dfrac{1}{L} & 0 \\ 0 & \dfrac{1}{L} \\ 0 & 0 \end{bmatrix} \tag{29}$$

### 4.2 Ultra-local model of the grid-connected PV system
To obtain the input–output form of the system (27), the two outputs $y_1 = v_{dc}$ and $y_2 = i_q$ are differentiated repeatedly until at least one input $u_1$ or $u_2$ appears explicitly in the expression of derivatives. This results in:

$$\begin{cases} \ddot{y}_1 = \dfrac{\dot{i}_{pv}}{C} - \dfrac{3}{Cx_3}\left(e_d\left(f_1 + \dfrac{1}{L}u_1\right) + e_q\left(f_2 + \dfrac{1}{L}u_2\right)\right) + \dfrac{3\left(e_dx_1 + e_qx_2\right)}{2Cx_3^2}f_3 + \dfrac{1}{C}\ddot{\varphi}_v \\ \dot{y}_2 = -\dfrac{R}{L}x_2 - wx_1 - \dfrac{e_q}{L} + \dfrac{1}{L}u_2 + \dfrac{1}{L}\dot{\varphi}_q \end{cases} \tag{30}$$

where $f_1$, $f_2$ and $f_3$ are given in (28).

The main limitation of controlling (30) using a model-based control technique is the need for the knowledge of the system parameters and disturbances that influence its behavior, as it is not easy to precisely identify the system uncertainties, external disturbances or electrical parameters or quantities. Moreover, the system parameters and the disturbances acting on the process can change during operation. This complicates practical implementation of a model-based controller and can significantly reduce control performance. Thus, in

order to address these issues, the dynamic model (30) is replaced by the following ultra-local model, as:

$$\begin{cases} \ddot{y}_1 = F_1 + \alpha_{11}u_1 + \alpha_{12}u_2 \\ \dot{y}_2 = F_2 + \alpha_{22}u_2 \end{cases} \tag{31}$$

where $F_1$ and $F_2$ include the unmodeled system dynamics, parametric uncertainty and external disturbances. $\alpha_{ij} \in \mathbb{R}$, $i = 1, 2$ and $j = 1, 2$, are design parameters to be selected by users. Both $F_1$ and $F_2$ are continuously updated to achieve a good estimation of the system dynamics and external disturbances. These estimates are valid for a short period of time and are considered within the closed-loop controller.

### 4.3 Controller design
The nonphysical model (31) is used here to design a MFC controller for the grid-connected PV system. The control law consists of two components: the first is a classical feedback controller and the second is a compensator for the effects of unmodeled system dynamics and external disturbances. Equation (31) can be rewritten in the following compact form, as:

$$\dot{y} = F + Du \tag{32}$$

where $y = [y_1, y_2]^T$ denotes the output vector, $u = [u_1, u_2]^T$ is the control input vector, $F = [F_1, F_2]^T$ represents the unmodeled system dynamics, and $D$ is the control gain matrix given by:

$$D = \begin{bmatrix} \alpha_{11} & \alpha_{12} \\ 0 & \alpha_{22} \end{bmatrix} \tag{33}$$

Defining the tracking errors by $e_1 = y_{r1} - y_1$ and $e_2 = y_{r2} - y_2$, or $e_1 = v_{dcr} - v_{dc}$ and $e_2 = i_{qr} - i_q$ where $v_{dcr}$ is generated by the MPPT tracker, the control objectives for the system (27) can be fulfilled with the following model-free control law:

$$u = D^{-1}\left( \underbrace{\begin{bmatrix} \ddot{y}_{r1} - \hat{F}_1 \\ \dot{y}_{r2} - \hat{F}_2 \end{bmatrix}}_{nonlinear\ compensation} + \underbrace{\begin{bmatrix} K_{p1}e_1 + K_{d1}\dfrac{de_1}{dt} \\ K_{p2}e_2 \end{bmatrix}}_{closed-loop\ tracking} \right) \tag{34}$$

Thus, the control input signals $u_1$ and $u_2$ can be regarded as the outputs of the i-PD and i-P controllers. $K_{p1}$ and $K_{p2}$, and $K_{d1}$ in (34) denote the proportional and the derivative gains, respectively. $\hat{F}_1$ and $\hat{F}_2$ in the nonlinearity compensator are the estimates of $F_1$ and $F_2$, and are computed as:

$$\begin{cases} \hat{F}_1 = \ddot{\hat{y}}_1 - \alpha_{11}u_1(t-h) - \alpha_{12}u_2(t-h) \\ \hat{F}_2 = \dot{\hat{y}}_2 - \alpha_{22}u_2(t-h) \end{cases} \quad (35)$$

where $\ddot{\hat{y}}_1$ and $\dot{\hat{y}}_2$ are the estimates of $\ddot{y}_1$ and $\dot{y}_2$. In this work, the online numerical differentiators used to provide the estimates $\ddot{\hat{y}}_1$ and $\dot{\hat{y}}_2$ are given by:

$$\begin{cases} \ddot{\hat{y}}_1 = \dfrac{60}{T_w^5}\displaystyle\int_0^{T_w}\left(T_w^2 - 6T_w\tau + \tau^2\right)y_1(t-\tau)d\tau \\ \dot{\hat{y}}_2 = \dfrac{6}{T_w^3}\displaystyle\int_0^{T_w}(T_w - 2\tau)y_2(t-\tau)d\tau \end{cases}$$

$$(36)$$

where $T_w$ denotes the width of the sliding window containing the output measurements of the system during the period $[t - T_w, t]$[36, 37]. The value of $T_w$ can be selected as an integral multiple of the sampling period, i.e., $T_w = MT_s$ where $M \in N^+$. In practice, the appropriate selection of $T_w$ needs to consider a trade-off between good estimation performance and noise attenuation.

Substituting (34) into (32), the dynamics of the tracking errors $e_1$ and $e_2$ are governed by:

$$\begin{cases} \ddot{e}_1 + K_{p1}e_1 + K_{d1}\dfrac{de_1}{dt} = \hat{F}_1 - F_1 \\ \dot{e}_2 + K_{p2}e_2 = \hat{F}_2 - F_2 \end{cases} \quad (37)$$

Consequently, if the unmodeled system dynamic $F_i$ is well estimated such that $\hat{F}_i - F_i \approx 0, i = 1, 2$, the dynamics of the tracking errors (37) can be expressed as

$$\begin{cases} \ddot{e}_1 + K_{p1}e_1 + K_{d1}\dfrac{de_1}{dt} = 0 \\ \dot{e}_2 + K_{p2}e_2 = 0 \end{cases} \quad (38)$$

This implies that the errors $e_1$ and $e_2$ converge asymptotically towards the origin. The control parameters $K_{p1}$, $K_{d1}$ and $K_{p2}$ are selected in order to stabilize the ideal dynamics of the tracking errors (38) and to achieve satisfactory tracking performance for both errors $e_1$ and $e_2$.

### 4.4 Simulation results

This subsection validates the designed model-free control scheme through an extensive simulation study using Matlab/Simulink. First, the controller performances are evaluated under normal conditions, defined by irradiation of 1 kW/m$^2$ and ambient temperature of

25 °C. To assess the robustness and disturbance rejection of the developed model-free controller, simulations are then performed under external disturbance (variable irradiance). The block diagram of the grid-connected PV system and its controller is depicted in Fig. 4. It consists of a PV generator, a three-phase grid, a DC/AC three-phase converter, a MPPT tracker and the MFC controller. The DC-link voltage reference $v_{dcr}$ is provided from the MPPT block based on the well-known Incremental Conductance (InC) MPPT method [4]. The desired $i_{qr}$ is set to 0 in order to have unity power factor. The two output control signals, $u_1$ and $u_2$ of the MFC controller, are used to provide the phase reference voltages which are used to generate the switching signals of the converter based on the conventional sinusoidal PWM.

The MFC controller (34) is implemented with a sampling time of $T_s = 4 \times 10^{-6}$ s, and the design parameters are selected as follows: $\alpha_{11} = -100$, $\alpha_{12} = -100$, $\alpha_{22} = 1000$ for the control gain matrix $D$, $K_{p1} = 5 \times 10^6$, $K_{d1} = 15 \times 10^2$, $K_{p2} = 4 \times 10^4$, and the width of the sliding window of the used online numerical differentiators (36) is $T_w = 250T_s$. The parameters of the grid-connected PV system are: grid voltage (RMS) $u = 220$ V, resistance of output filter $R = 0.1\,\Omega$ and inductance $L = 8$ mH, DC-link capacitance $C = 5$ mF and switching frequency $F_s = 10$ kHz. In the design, the grid-connected PV system model is assumed to be completely unknown and the controller does not require the knowledge of the system parameters as is needed in conventional model-based controllers. In fact, only the dynamic model, the system parameters and those in Table 1 are required for simulation purposes.
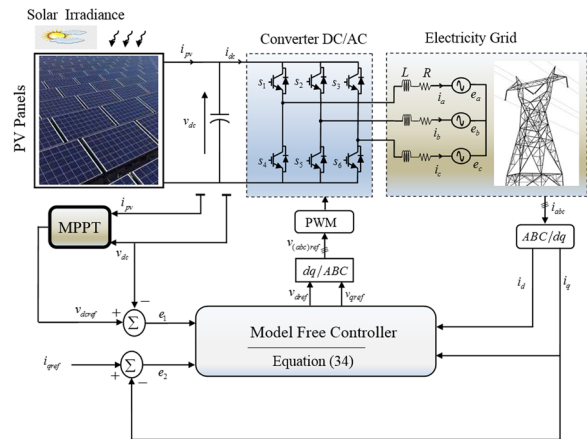


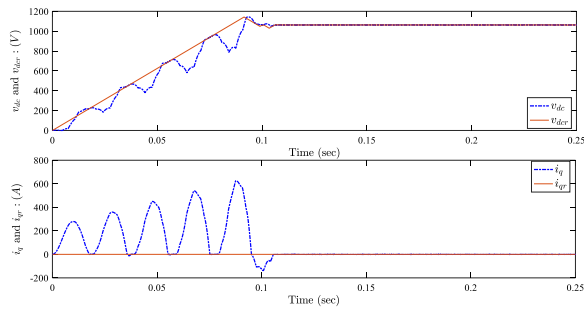**Fig. 4** Proposed MFC controller applied to the grid-connected PV system

**Fig. 5** Operation under normal conditions: Top. DC link voltage $v_{dc}$ (V) (dotted line) and its reference $v_{dcr}$ (solid line). Bottom. Current $i_q$ (A) (dotted line) and its reference $i_{qr}$ (solid line)
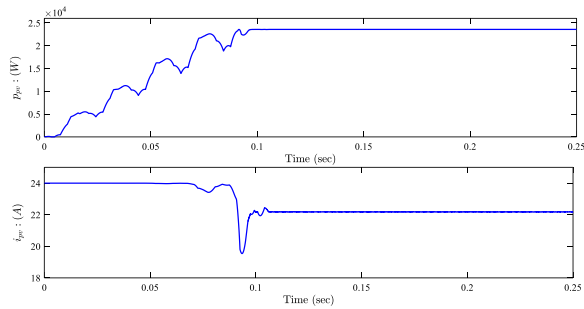


**Fig. 6** Operation under normal conditions: Top. PV generator output power $p_{pv}$ (W). Bottom. PV generator output current $i_{pv}$ (A)
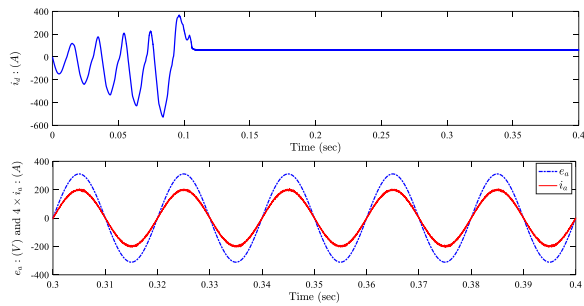


**Fig. 7** Operation under normal conditions: Top. Current $i_d$ (A). Bottom. Grid current and voltage waveforms: Current $4 \times i_a$ (A) (solid line) and voltage $e_a$ (V) (dotted line)



**Fig. 8** Operation under normal conditions: Top. Estimate $\dot{\hat{y}}_2$. Bottom. Estimate $\ddot{\hat{y}}_1$
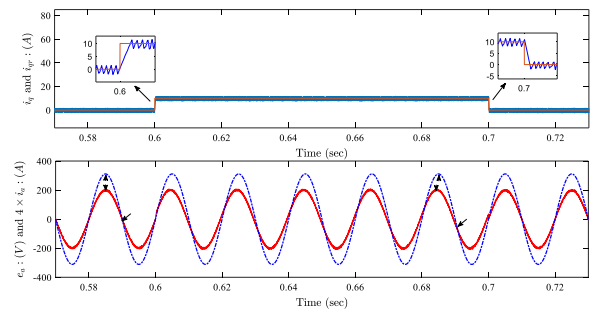


**Fig. 9** Operation under normal conditions with step change in $i_{qr}$: Top. Current $i_q$ (A) (dotted line) and its reference $i_{qr}$ (solid line). Bottom. Grid current and voltage waveforms: Current $4 \times i_a$ (A) (solid line) and voltage $e_a$ (V) (dotted line)
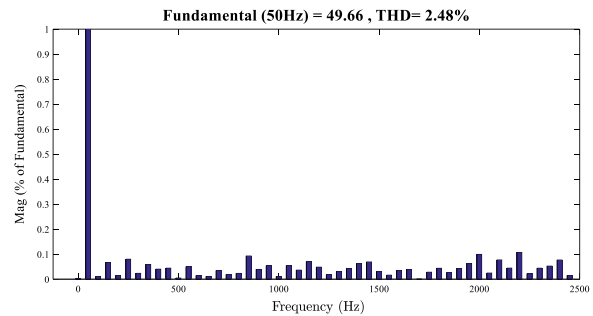


**Fig. 10** Harmonic spectrum of the current injected into electrical grid

### 4.4.1 Operation under normal conditions

The experimental results under normal conditions are reported in Figs. 5, 6, 7, 8, 9, 10. The DC-link voltage $v_{dc}$ and its reference $v_{dcr}$ are illustrated in Fig. 5 (top), and the current $i_q$ and its reference $i_{qr}$ are given in Fig. 5 (bottom). From these results, it can be seen that the DC-link voltage tracks the reference signal generated by the MPPT algorithm, while the current $i_q$ also converges to its reference and remains approximately zero after a short transient time (about 0.1 s). Figures 5 and 6 (top) show that the output power, voltage and current of the PV generator converge with a short response time to the maximum power point defined by $P = 23584$ W, $v_{dc} = 1066$ V and $I = 22.13$ A. The $d-$axis grid current tends to a constant value as illustrated in Fig. 7 (top), while the grid current and voltage waveforms displayed in Fig. 7 (bottom) confirm that both are sinusoidal and synchronized, which implies unity power factor.

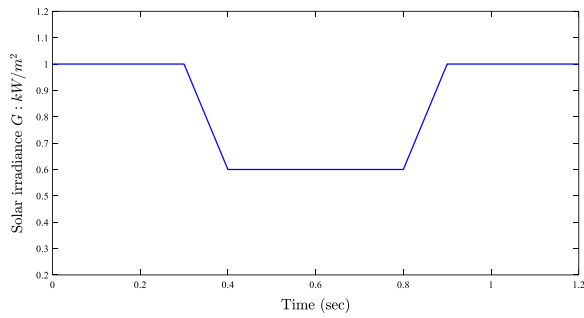The time evolutions of the two estimates $\ddot{\hat{y}}_1$ and $\dot{\hat{y}}_2$ used to continuously adapt $\hat{F}_1$ and $\hat{F}_2$ are depicted in Fig. 8.

**Fig. 11** Solar Irradiance $G$ versus time (s)



**Fig. 13** Operation under variable irradiance: Top. PV generator output power $p_{pv}$ (W). Bottom. PV generator output current $i_{pv}$ (A)
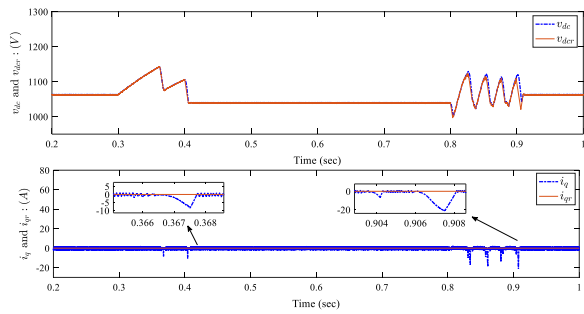


**Fig. 12** Operation under variable irradiance: Top. DC link voltage $v_{dc}$ (V) (dotted line) and its reference $v_{dcr}$ (solid line). Bottom. Current $i_q$ (A) (dotted line) and its reference $i_{qr}$ (solid line)



**Fig. 14** Operation under variable irradiance: Top. Current $i_d$ (A). Bottom. Grid current and voltage waveforms: Current $4 \times i_a$ (A) (solid line) and voltage $e_a$ (V) (dotted line)

System behavior for a step change in current reference $i_{qr}$ applied at 0.6 s is illustrated in Fig. 9. As seen from Fig. 9 (top), the current $i_q$ rapidly reaches its new reference of 10 A, and consequently, the grid current and voltage become out of phase. However, when the reference $i_{qr}$ is back to 0 at 0.7 s, the current $i_q$ follows this new value and the grid current and voltage are again in phase as shown in Fig. 9 (bottom). The harmonic spectrum of the current injected into the grid is displayed in Fig. 10. As seen, the low order harmonics are attenuated, the THD is less than 5% and each individual harmonic is also very low compared to the limits in the IEEE standards [38].

### 4.4.2 Operation under external disturbance (variable irradiance)

Here the performance of the MFC controller when operating under a rapid change in solar irradiance is examined. The scenario adopted in this test for solar irradiance variation is depicted in Fig. 11. Simulation in the presence of radiation changes using the control law (34) without the nonlinear compensation term, in order to elucidate the important role of the real-time update of the local model. The results of the test under variable irradiance are shown in Figs. 12, 13, 14, 15, 16. From these results, it can be seen that any decrease/increase in irradiance $G$
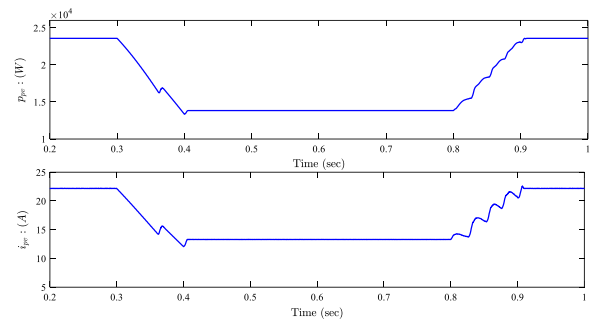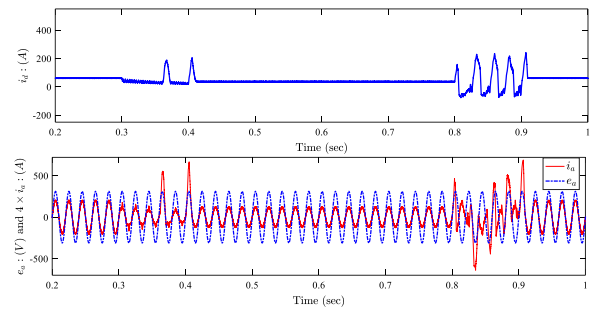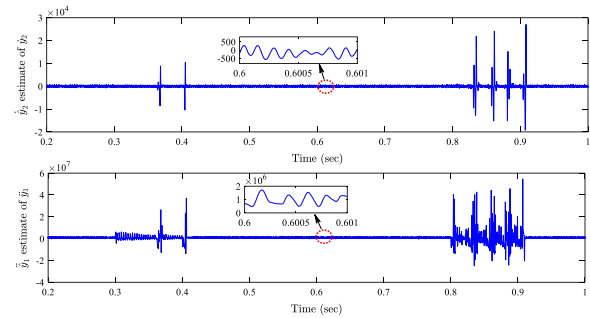


**Fig. 15** Operation under variable irradiance: Top. Estimate $\dot{\hat{y}}_2$. Bottom. Estimate $\ddot{\hat{y}}_1$

leads to a decrease/increase of the voltage, the current and the power of the PV generator, which allows it to quickly reach the instantaneous MPP.

The controlled system with the MFC controller exhibits a fast transient behavior under sudden change in solar irradiance as illustrated by Figs. 12 and 14 (bottom). The MFC forces the DC link voltage $v_{dc}$ to rapidly attain its updated reference in order to reach the new MPP. Moreover, the time evolution of the q-axis grid current,
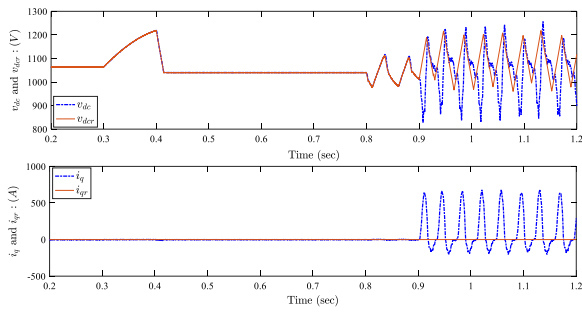
**Fig. 16** MFC without nonlinear compensation: Top. DC link voltage $v_{dc}$ (V) (dotted line) and its reference $v_{dcr}$ (solid line). Bottom. Current $i_q$(A) (dotted line) and its reference $i_{qr}$ (solid line)



**Fig. 17** Comparative study: Top. DC link voltage $v_{dc}$ (V) (dotted line) and its reference $v_{dcr}$ (solid line) with MFC controller. Bottom. Dc link voltage $v_{dc}$ (V) (dotted line) and its reference $v_{dcr}$ (solid line) with IOFLC controller

illustrated in Fig. 12 (bottom), reveals that $i_q$ is not influenced by solar irradiance changes. This means that the power factor is not affected and remains unity. Figure 14 (bottom) shows that despite the effect of the external disturbance (change in solar irradiance) the grid current and voltage remain in phase.

In Fig. 15, it is noted that the estimates $\ddot{\hat{y}}_1$ and $\dot{\hat{y}}_2$ change according to the variation of solar irradiance $G$, This allows the updating of the terms $\hat{F}_1$ and $\hat{F}_2$. Figure 16 describes the results achieved using the MFC controller without nonlinear compensation. As can be seen, because of the effect of variation in solar irradiance, both the DC-link voltage $v_{dc}$ and current $i_q$ do not follow their reference curves from 0.9 s, which proves the important role that the nonlinear compensation term plays in control performance and in dealing with unknown uncertainties. Indeed, the real-time update of $\hat{F}_1$ and $\hat{F}_2$ in the nonlinear compensation term, based on the numerical differentiator (36), significantly improves the efficiency and the robustness of the MFC controller against system parameter uncertainties and external disturbances.

### 4.4.3 Comparison with a model-based controller

Finally, in order to examine the performance of the proposed model-free control scheme for a grid-connected PV system, a comparative study is conducted between the proposed controller and the model-based Input Output Feedback Linearization Control (IOFLC) introduced in [4]. This comparative study is performed with the same simulation parameters and under the same atmospheric conditions, at an ambient temperature of 25 °C and with a variable irradiance $G$ as in Fig. 11. As can be observed in Figs. 17 and 18, the obtained curves of the DC-link voltage $v_{dc}$ and current $i_q$ highlight the superiority of the tracking performance achieved with the MFC controller over the IOFLC controller [4]. The transient behavior with the MFC controller is faster
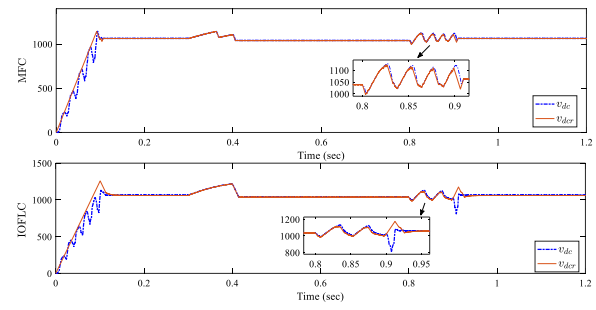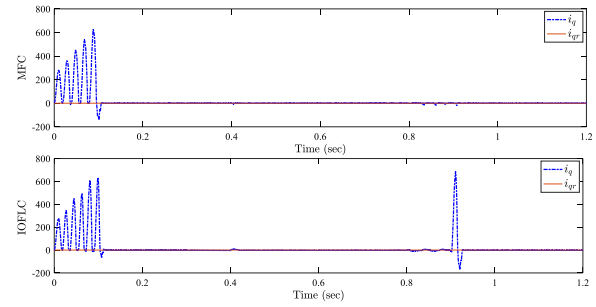


**Fig. 18** Comparative study: Top. Current $i_q$ (A) (dotted line) and its reference $i_{qr}$ (solid line) with MFC controller. Bottom. Current $i_q$ (A) (dotted line) and its reference $i_{qr}$ (solid line) with IOFLC controller

**Table 2** Comparisons of tracking errors performance $e_1 = v_{dcr} - v_{dc}$ and $e_2 = i_{qr} - i_q$

| Control strategy | Average of (abs($e_i$)) | Range of $e_i$ | Standard deviation of $e_i$ |
|---|---|---|---|
| *MFC* | | | |
| $e_1$ | 1.53 | $(-54.59, 4)$ | 4.40 |
| $e_2$ | 0.98 | $(-2.50, 21.08)$ | 1.38 |
| *IOFLC* [4] | | | |
| $e_1$ | 6.82 | $(-34.32, 308.18)$ | 23.446 |
| $e_2$ | 8.56 | $(-686.33, 170.22)$ | 53.07 |

than the IOFLC controller. In addition, the tracking performance of the grid-connected PV system with the MFC controller is less sensitive to the effect of the irradiance variation than the IOFLC controller.

A qualitative comparison between the MFC controller and the IOFLC controller has also been performed and the results are summarized in Table 2. The main characteristics of the tracking errors $e_1 = v_{dcr} - v_{dc}$ and

$e_2 = i_{qr} - i_q$ obtained by the two different implementation methods are used to examine the performance of each controller in the time interval of [0.2 s, 1.2 s].

The average absolute values of the errors $e_i$, $i = 1, 2$, over the duration of the test, the range of $e_i$ as well as the standard deviation of $e_i$ are used as performance indices. From the results in Table 2, it is clear that the proposed MFC control scheme achieves a better closed-loop system performance than the IOFLC controller.

## 5 Conclusion

In this paper, the problem of controlling grid-connected PV systems is considered using a model-free control scheme based on a numerical differentiator. A continuously updated local model is used to estimate the unknown nonlinear dynamics of the overall system. An efficient model-free control law is designed using the updated local model to achieve the control objectives. The ability and the performance of the proposed MFC controller have been examined through in-depth simulations supplemented by comparative studies. These have shown that the closed-loop system response with the MFC controller exhibits good tracking performance and robustness against external disturbances. Future work will focus on the extension of the designed model-free control scheme to a grid-connected hybrid wind/PV distributed generation system.

## Abbreviations

$R_s$: Series resistance; $R_{sh}$: Shunt resistance; $i_{pv}$: PV output current; $v_{dc}$: PV output voltage; $i_{ph}$: Generated photocurrent; $G$: Solar irradiance; $T$: Cell's working temperature; $i_D$: Current through the diode; $i_{sh}$: Current flowing through the resistor $R_{sh}$; $I_0$: Cell's reverse saturation current; $q$: Electron charge; $n$: Duality factor of the diode; $K$: Boltzmans constant; $N_s$: Series cells; $N_p$: Parallel cells; $i_{sc}$: Short circuit current at reference temperature and radiation; $I_{0R}$: Cell reverse saturation current at the reference temperature $T_{ref}$; $k_i$: Short circuit current temperature coefficient; $E_g$: Band-gap of the semiconductor used in the cell; $v_{a,b,c}$: Three-phase voltage of the converter; $i_{a,b,c}$: Three-phase current injected into the grid; $e_{a,b,c}$: Three-phase line voltage of the grid; $R$: Total resistance of the filter; $L$: Total inductance of the filter; $C$: DC-link capacitance; $i_{d,q}$: D-q components of the grid current; $v_{d,q}$: D-q components of the output voltage of the converter; $e_{d,q}$: D-q components of the grid voltage; $f$: Grid frequency; $\varphi_{d,q}$: Disturbance terms in phase currents; $\alpha$: Non-physical constant parameter; $v$: Order of derivative; $u$: Control input vector; $F$: Unmodeled system dynamics; $D$: Control gain matrix.

## Authors' contributions

AB: Conceptualization, data curation, formal analysis, investigation, methodology, project administration, resources, software, validation, visualization, writing—original draft. S-AT: supervision, validation, visualization, writing—review & editing. SL: conceptualization, formal analysis, investigation, methodology, supervision, validation, visualization, writing—review & editing. NB: Supervision, visualization, writing—review & editing. All authors read and approved the final manuscript.

## Authors' Information

Ahsene Boubakir (1981-) male, Ph.D. and associate professor, the main research direction isrenewable energy, adaptive control, model-free control and sliding mode control.
Sid-Ahmed Touil (1991-) male, Ph.D. and assistant professor, the main research direction is electromagnetic compatibility in power electronics, control of power converters and renewable energy.
Salim Labiod (1972-) male, Ph.D. and professor, the main research direction is fuzzy/neural control, nonlinear control, adaptive control and fault tolerant control systems.
Nasserdine Boudjerda (1964-) male, Ph.D. and professor, the main research direction is electromagnetic compatibility in power electronics, control of power converters and renewable energy.

## Availability of data and materials

Not applicable.

## Declarations

## Competing interests

The authors declare that they have no known competing financial interests or personal relationships that could have appeared to influence the work reported in this paper.

## Author details

[1]LAJ, Faculty of Science and Technology, University of Jijel, BP. 98, Ouled Aissa, 18000 Jijel, Algeria. [2]Department of Electrical Engineering, University of Jijel, Jijel, Algeria. [3]LER, Faculty of Sciences and Technology, University of Jijel, BP 98, Ouled Aissa, 18000 Jijel, Algeria.

## References

1. Alajmi, B. N., Ahmed, K. H., Finney, S. J., & Williams, B. W. (2011). Fuzzy-logic-control approach of a modified hillclimbing method for maximum power point in microgrid stand-alone photovoltaic system. *IEEE Transactions on Power Electronics, 26*(4), 1022–1030.
2. Chong, L. W., Wong, Y. W., Rajkumar, R. K., & Isa, D. (2018). An adaptive learning control strategy for stand-alone PV system with battery-supercapacitor hybrid energy storage system. *Journal of Power Sources, 394*, 35–49.
3. Muhsen, D. H., Nabil, M., Haider, H. T., & Khatib, T. (2019). A novel method for sizing of stand-alone photovoltaic system using multi-objective differential evolution algorithm and hybrid multi-criteria decision making methods. *Energy, 174*, 1158–1175.
4. Lalili, D., Mellit, A., Lourci, N., Medjahed, B., & Berkouk, E. (2011). Input output feedback linearization control and variable step size MPPT algorithm of a grid-connected photovoltaic inverter. *Renewable Energy, 36*(12), 3282–3291.
5. Merabet, A., Labib, L., Ghias, A. M. Y. M., Ghenai, C., & Salameh, T. (2017). Robust feedback linearizing control with sliding mode compensation for a grid-connected photovoltaic inverter system under unbalanced grid voltages. *IEEE Journal of Photovoltaics, 7*(3), 828–838.
6. Aourir, M., Abouloifa, A., Lachkar, I., Aouadi, C., Giri, F., & Guerrero, J. M. (2020). Nonlinear control and stability analysis of single stage grid-connected photovoltaic systems. *International Journal of Electrical Power & Energy Systems, 115*, 105439.
7. Selvaraj, J., Rahim, N. A., & Krismadinata, C. (2008). Digital PI current control for grid connected PV inverter. In Proceedings of the 2008 3rd IEEE conference on industrial electronics and applications, Singapore, June 3–5, 2008 (pp. 742–746).

8.  Mnati, M., Bozalakov, D., & Van den Bossche, A. (2018). PID control of a three phase photovoltaic inverter tied to a grid based on a 120-degree bus clamp PWM. *IFAC-PapersOnLine, 51*, 388–393.

9.  Flores, J. V., Pereira, L. F. A., Bonan, G., Coutinho, D. F., & Gomes da Silva, J. M. (2016). A systematic approach for robust repetitive controller design. *Control Engineering Practice, 54*, 214–222.

10. Merabet, A., Labib, L., & Ghias, A. M. Y. M. (2018). Robust model predictive control for photovoltaic inverter system with grid fault ride-through capability. *IEEE Transactions on Smart Grid, 9*(6), 5699–5709.

11. Sabir, A., & Javaid, M. S. (2018). Robust control of grid-connected photovoltaic systems under unbalanced faults without PLL. *Canadian Journal of Electrical and Computer Engineering, 41*(4), 179–190.

12. Errouissi, R., Al-Durra, A., & Muyeen, S. M. (2016). Offset-free feedback linearization control of a three-phase grid-connected photovoltaic system. *IET Power Electronics, 9*, 1–20.

13. Merabet, A., Labib, L., Ghias, A. M., Aldurra, A., & Debbouza, M. (2019). Dual-mode operation based second-order sliding mode control for grid-connected solar photovoltaic energy system. *International Journal of Electrical Power & Energy Systems, 111*, 459–474.

14. Guo, B., Su, M., Wang, H., Tang, Z., Liao, Y., Zhang, L., & Shi, S. (2020). Observer-based second-order sliding mode control for grid-connected VSI with LCL-type filter under weak grid. *Electric Power Systems Research, 183*, 106270.

15. Menadi, A., Abdeddaim, S., Ghamri, A., & Betka, A. (2015). Implementation of fuzzy-sliding mode based control of a grid connected photovoltaic system. *ISA Transactions, 58*, 586–594.

16. Priyadarshi, N., Sanjeevikumar, P., Bhaskar Ranjana, M., Blaabjerg, F., & Sharma, A. (2018). A fuzzy SVPWM based inverter control realization of grid integrated PV-Wind system with FPSO MPPT algorithm for a grid-connected PV/Wind power generation system: Hardware implementation. *IET Electric Power Applications, 12*(7), 1–10.

17. Roselyn, J. P., Chandran, C. P., Nithya, C., Devaraj, D., Venkatesan, R., Gopal, V., & Madhura, S. (2020). Design and implementation of fuzzy logic based modified real-reactive power control of inverter for low voltage ride through enhancement in grid connected solar PV system. *Control Engineering Practice, 101*, 104494.

18. Touil, S.-A., Boudjerda, N., Boubakir, A., & El Khamlichi Drissi, K. (2019). A sliding mode control and artificial neural network based MPPT for a direct grid-connected photovoltaic source. *Asian Journal of Control, 21*(4), 1892–1905.

19. Sabir, A., & Ibrir, S. (2020). A robust control scheme for grid-connected photovoltaic converters with low-voltage ride-through ability without phase-locked loop. *ISA Transactions, 96*, 287–298.

20. Dhar, S., & Dash, P. (2016). A new backstepping finite time sliding mode control of grid connected PV system using multivariable dynamic VSC model. *International Journal of Electrical Power & Energy Systems, 82*, 314–330.

21. Zangeneh Bighash, E., Sadeghzadeh, S. M., Ebrahimzadeh, E., & Blaabjerg, F. (2018). High quality model predictive control for single phase grid-connected photovoltaic inverters. *Electric Power Systems Research, 158*, 115–125.

22. Golzari, S., Rashidi, F., & Farahani, H. F. (2019). A lyapunov function based model predictive control for three phase grid connected photovoltaic converters. *Solar Energy, 181*, 222–233.

23. Mohamed, A. A., Metwally, H., El-Sayed, A., & Selem, S. (2019). Predictive neural network based adaptive controller for grid-connected PV systems supplying pulse-load. *Solar Energy, 193*, 139–147.

24. Barra, K., & Rahem, D. (2014). Predictive direct power control for photovoltaic grid connected system: An approach based on multilevel converters. *Energy Conversion and Management, 78*, 825–834.

25. Ouchen, S., Abdeddaim, S., Betka, A., & Menadi, A. (2016). Experimental validation of sliding mode-predictive direct power control of a grid connected photovoltaic system feeding a nonlinear load. *Solar Energy, 137*, 328–336.

26. Bp solar. (2003). Datasheet of 160 Watt Photovoltaic Module BP 3160. https://www.solarelectricsupply.com /bp-3160-solar-pv-modules-596.

27. Fakham, H., Lu, D., & Francois, B. (2011). Power control design of a battery charger in a hybrid active PV generator for load-following applications. *IEEE Transactions on Industrial Electronics, 58*(1), 85–94.

28. Fliess, M., & Join, C. (2009). Model-free control and intelligent PID controllers: Towards a possible trivialization of nonlinear control? *IFAC Proceedings Volumes, 42*(10), 1531–1550.

29. Fliess, M., & Join, C. (2013). Model-free control. *International Journal of Control, 86*(12), 2228–2252.

30. MohammadRidha, T., Aït-Ahmed, M., Chaillous, L., Krempf, M., Guilhem, I., Poirier, J., & Moog, C. H. (2018). Model-free iPID control for glycemia regulation of type-1 diabetes. *IEEE Transactions on Biomedical Engineering, 65*(1), 199–206.

31. Isidori, A. (1995). *Nonlinear control systems*. Springer.

32. Khalil, H. K. (2002). *Nonlinear systems* (3rd ed.). Prentice-Hall.

33. Join, C., Delaleau, E., Fliess, M., & Moog, C. H. (2017). Discussing an intriguing result on model-free control. *Automatique Control, 1*(1), 1–9.

34. D'Andréa-Novel, B., Fliess, M., Join, C., Mounier, H., & Steux, B. (2010). A mathematical explanation via intelligent PID controllers of the strange ubiquity of PIDs. In: 18th Mediterranean Conference on Control and Automation, MED'10, Marrakech, Morocco, June 23–25, 2010 (pp. 395–400).

35. Fliess, M., Join, C., & Sira-Ramirez, H. (2008). Non-linear estimation is easy, International Journal of Modelling. *Identification and Control, 4*(1), 12–27.

36. Mboup, M., Join, C., & Fliess, M. (2009). Numerical differentiation with annihilators in noisy environment. *Numerical Algorithms, 50*(4), 439–467.

37. Wang, Z., & Wang, J. (2020). Ultra-local model predictive control: A model-free approach and its application on automated vehicle trajectory tracking. *Control Engineering Practice, 101*, 104482.

38. IEEE Std 1547–2003 (2003). IEEE Standard for Interconnecting Distributed Resources with Electric Power Systems. 1–28.